Doping Profile Effects on Device Characteristics of Nano-Scale MOSFETs

Hiroshi Takeda and Nobuya Mori

Department of Electronic Engineering, Osaka University
2-1 Yamada-oka, Suita City, Osaka 565-0871, Japan
Tel: +81-6-6879-7767, Fax: +81-6-6879-7753
E-mail: takeda@ele.eng.osaka-u.ac.jp

Abstract – **We have numerically simulated device characteristics of sub-10 nm gate length bulk *n*-MOSFETs with various doping profiles, using a quantum transport simulator based on a non-equilibrium Green's function method. Comparing the simulated results, we study effects of the doping profile on the device characteristics. The simulation study reveals that the off-set doping profiles in the source/drain regions play an important role in controlling the direct source-to-drain tunneling current.**

1 Introduction

The device dimensions of MOSFETs have been shrunk into deep sub-100 nm regime. At the research level, several sub-10 nm gate length MOSFETs have been reported [1–3]. In recent years, non-conventional multiple-gate MOSFETs [4–6], such as double-gate SOI MOSFETs and FinFETs, have received great attention for their significant suppression of the short channel effects. The normal operation of sub-10 nm planar bulk-MOSFETs have, however, been reported [1]. Thus, nano-scale planar bulk-MOSFETs will still be one of the key components in future ULSI systems.

In nano-scale MOSFETs, quantum mechanical effects, such as direct source-to-drain (SD) tunneling and subband quantization effects along the gate confinement direction, influence the carrier transport properties. Especially, the direct SD-tunneling current, which greatly increases in short channel length devices, directly degrades the sub-threshold characteristics. In bulk-MOSFETs, well-designed doping profiles may overcome the degradation of the sub-threshold characteristics because the transport properties are significantly affected by the doping profile. In order to design the doping profiles of nano-scale MOSFETs, it is essential to simulate the device characteristics within a quantum transport method. In the present study, we have performed a quantum transport simulation based on a non-equilibrium Green's function (NEGF) method [7–9], which can naturally handle the quantum mechanical effects with open boundary conditions. By comparing simulated results of devices with a variety of doping profiles, we study effects of the doping profile on the device characteristics in sub-10 nm bulk-MOSFETs.

2 Simulation Method and Device Structure

We have simulated transport characteristics of the devices shown in Fig. 1. We define the x- and the z-direction as the source-drain direction and the gate confinement direction, respectively. Along the channel width direction, the system is assumed to be uniform and the periodic boundary condition is applied. We have self-consistently solved NEGF transport equations based on a coupled-mode space method [7, 8] and the two-dimensional Poisson equation. In solving the NEGF transport equations, we neglect scatterings and assume the ballistic transport condition. The Poisson equation is solved with the Dirichlet boundary condition for the gate region and the Neumann boundary condition for other regions. Semi-infinite equilibrium reservoirs are assumed to be connected at the edges of the source/drain regions. The Fermi levels of the source/drain reservoirs are determined by the applied source/drain voltage. The Fermi level of the source reservoir, E_f^S, is set to be 0 eV.

Doping profile of the simulated device is given by the formulae for the well-tempered bulk Si n-MOSFETs [10]. The n- and p-type doping profiles, $n(x,z)$ and $p(x,z)$, are written as

$$n(x,z) = n_0 \times [f_n(x - x_c) + f_n(x_c - x)] \times g_n(z), \quad (1)$$

$$p(x,z) = p_0 \times \left[f_p(x - x_c) + f_p(x_c - x)\right] \times g_p(z), \quad (2)$$

where x_c is the x-coordinate of the center of the gate. n_0 and

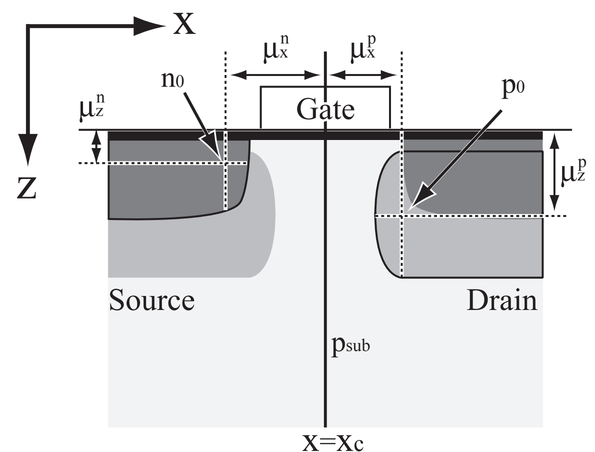

Figure 1: Schematic diagram of the device structure and the doping profiles. n_0 and p_0 are the peak doping concentrations. $\mu_x^{n/p}$ and $\mu_z^{n/p}$ are the centers of the Gaussian distributions along the x- and the z-direction, respectively. The half-Gaussian distributions are assumed along the x-direction.

p_0 are the peak doping concentrations of the n- and p-type regions, respectively. $f_{n/p}(x)$ and $g_{n/p}(z)$ are the distribution functions defined by

$$f_{n/p}(x) = \begin{cases} \exp\left[-\left(\frac{x-\mu_x^{n/p}}{\sigma_x^{n/p}}\right)^2\right] & (|x| \le \mu_x^{n/p}) \\ 1 & (|x| > \mu_x^{n/p}) \end{cases}, \quad (3)$$

$$g_{n/p}(z) = \exp\left[-\left(\frac{z-\mu_z^{n/p}}{\sigma_z^{n/p}}\right)^2\right]. \quad (4)$$

Here, $\mu_x^{n/p}$ is the center of the half-Gaussian distribution along the x-direction and $\mu_z^{n/p}$ is the center of the Gaussian distribution along the z-direction. The constant distribution is assumed for $|x - x_c| \ge \mu_x^{n/p}$. $\sigma_x^{n/p}$ and $\sigma_z^{n/p}$ represent the standard deviations of the distribution along the x- and the z-direction, respectively. Changing these doping parameters, we simulated devices with various doping profiles.

3 Results and Discussion

Figure 2 shows the calculated I_d–V_g characteristics of 9 nm gate length MOSFETs at V_d = 0.4 V. Thickness of the gate oxide (SiO_2) layer is 0.93 nm and the gate electrode is assumed to be n-type poly-Si. The doping profile parameters are $n_0 = 2.0 \times 10^{20}\,\mathrm{cm}^{-3}$, $p_0 = 8.0 \times 10^{19}\,\mathrm{cm}^{-3}$, μ_x^n = 4.5 nm and $\mu_z^n = \mu_z^p$ = 0 nm. The p-type doping center along the x-direction, μ_x^p, is varied from 0.5 nm to 5.5 nm. Other parameters are σ_x^n = 0.67 nm, σ_x^p = 1.33 nm and $\sigma_z^n = \sigma_z^p$ = 9.0 nm. The doping concentration of the p-type substrate is $10^{17}\,\mathrm{cm}^{-3}$. As shown in Fig. 2, the sub-threshold characteristics becomes better for smaller μ_x^p. The drive current is, however, very small for smaller μ_x^p. This is due to strong confinement at the channel region caused by high p-type doping concentrations for smaller μ_x^p. The left panel of Fig. 3 shows the lowest subband energy profiles along the x-direction at the off-state (V_g = 0 V). For smaller μ_x^p, the channel barrier becomes high enough for sufficiently small off-current, although this high channel barrier significantly reduces the on-current.

Figure 4 shows I_d–V_g curves of the same devices as Fig. 2 but with a constant μ_x^p = 3.5 nm and various μ_x^n ranged from 2.5 nm to 6.5 nm. Trade-off relationship between the sub-threshold and the on-current characteristics can be seen in Fig. 4. In the right panel of Fig. 3, where the off-state lowest subband profiles for each μ_x^n are plotted, we see that μ_x^n affects not only the hight of the channel barrier but also the barrier thickness. As a result, μ_x^n influences the device characteristics more significantly than μ_x^p.

To find out what doping profiles are suitable for sub-10 nm bulk-MOSFETs, we have simulated μ_x^n dependence of device characteristics with a fixed off-current I_{off} = 5.45 μA/μm at V_g = 0 V. I_{off} = 5.45 μA/μm is obtained in the device with μ_x^n = 4.5 nm and μ_x^p = 3.5 nm as shown in Figs. 2 and 4, and the parameter μ_x^p is adjusted to obtain this value for each devices with varied μ_x^n. Other parameters are the same as those used in Figs. 2 and 4. In Fig. 5, μ_x^n dependence of the sub-threshold slope is plotted by closed circles. It can be seen that the sub-threshold slope is 150 mV/dec at μ_x^n = 9.5 nm and it degrades to 260 mV/dec at μ_x^n = 3.5 nm. This degradation of the sub-threshold slope can be attributed to the direct SD-tunneling current. Figure 6 shows μ_x^n dependence of the SD-tunneling current ratio to whole drain current (closed circles) and effective channel length (open circles) at V_g = 0 V. Here, we define the SD-tunneling current as the current component having the energy region below the maximum subband energy, E_{top}, and the effective channel length as the width of the channel barrier at the energy

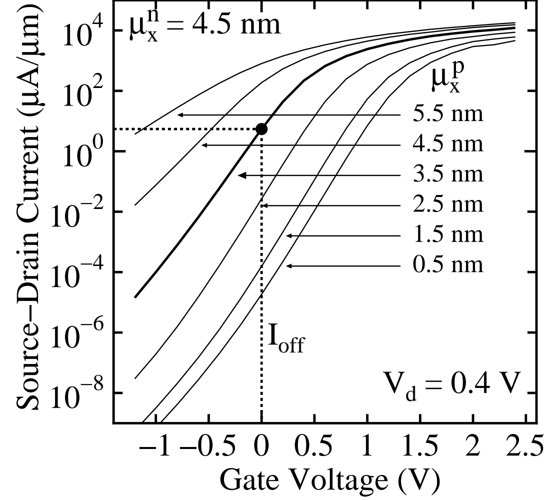

Figure 2: Simulated I_d–V_g curves of 9 nm gate length MOSFETs with μ_x^n = 4.5 nm and μ_x^p = 0.5 – 5.5 nm at V_d = 0.4 V. At V_g = 0 V, the off-current is I_{off} = 5.45 μA/μm for μ_x^n = 4.5 nm and μ_x^p = 3.5 nm.

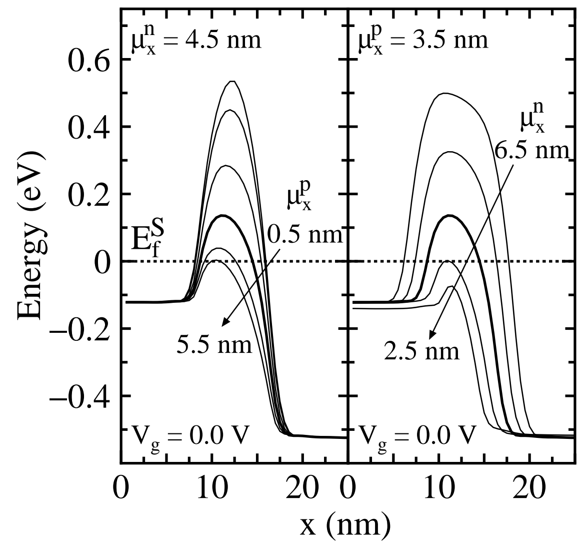

Figure 3: Lowest subband energy profiles at V_g = 0 V for the devices with μ_x^n = 4.5 nm and μ_x^p = 0.5 – 5.5 nm (left), and μ_x^n = 2.5 – 6.5 nm and μ_x^p = 3.5 nm (right). Dotted line represents the Fermi energy of the source reservoir.

of $(E_{top} - E_{source})/2$ with E_{source} being the subband energy at the source edge. For smaller μ_x^n, it is found that the SD-tunneling current dominates the off-state device characteristics with very short effective channel length. For example, at $\mu_x^n = 3.5$ nm, the effective channel length is 4 nm, and the tunneling current ratio exceeds 80 %. On the other hand, the tunneling current ratio is only 10 % at $\mu_x^n = 9.5$ nm with 12 nm effective channel length. Thus, in sub-10 nm MOSFETs, off-set doping profiles of $\mu_x^n > L_g/2$ is required in order to reduce the degradation of the sub-threshold characteristics.

Figure 5 shows μ_x^n dependence of the sub-threshold slope for $\sigma_z^n = 11$ nm and $\mu_z^p = 12$ nm (open squares) and for $\sigma_z^n = 7.0$ nm and $\mu_z^p = 8.0$ nm (open triangulars). It can be seen from Fig. 5 that almost the same sub-threshold slope is obtained for larger μ_x^n, although a better sub-threshold slope is obtained in devices with smaller σ_z^n and smaller μ_x^n. At $\mu_x^n = 3.5$ nm, the sub-threshold slopes are 220 mV/dec for $\sigma_z^n = 7.0$ nm, 260 mV/dec for $\sigma_z^n = 9.0$ nm, and 290 mV/dec for $\sigma_z^n = 11$ nm. In the device with smaller σ_z^n, the p-type doping concentration becomes relatively high at around the source/channel and the channel/drain boundaries due to the low n-type doping densities of the source and the drain regions. Thus, for smaller σ_z^n, the devices has less SD-tunneling current because the channel barrier rises and falls down a little closer to the source/drain regions. For instance, the SD-tunneling current ratios are 90 % for $\sigma_z^n = 11$nm, 84 % for $\sigma_z^n = 9.0$nm and 77 % for $\sigma_z^n = 7.0$nm at $\mu_x^n = 3.5$ nm. Note that this slight difference of the channel barrier around the source/channel and the channel/drain boundaries less affects for larger μ_x^n because of the long effective channel.

Figure 7 shows the on-current, I_{on}, at $V_g = V_d = 0.4$ V as a function of μ_x^n for $\sigma_z^n = 11$ nm (open squares), $\sigma_z^n = 9.0$ nm (closed circles), and $\sigma_z^n = 7.0$ nm (open triangulars).

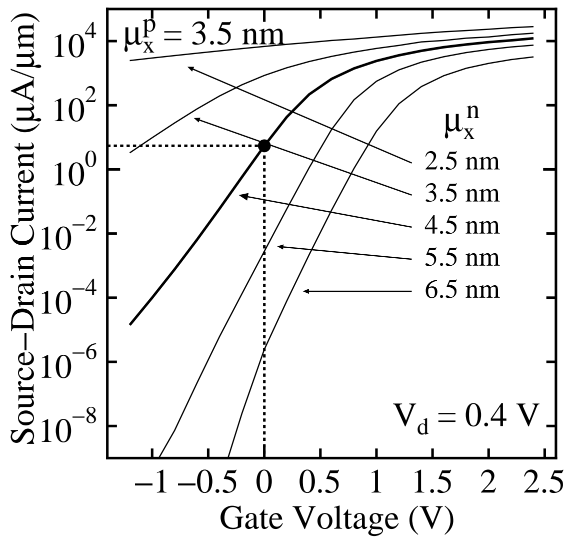

Figure 4: Simulated I_d–V_g curves of the devices with $\mu_x^n = 3.5$ nm and $\mu_x^p = 2.5 - 6.5$ nm at $V_d = 0.4$ V.

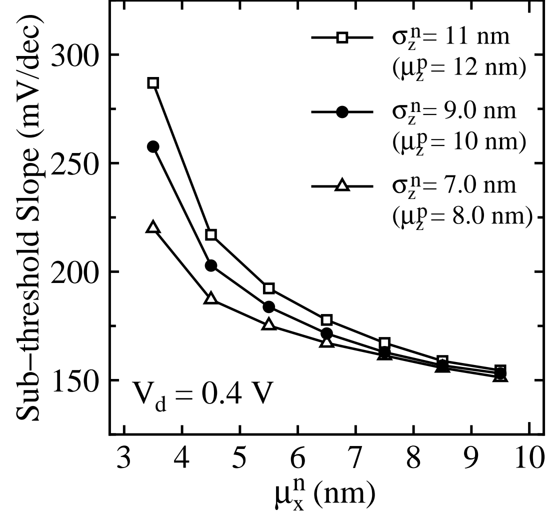

Figure 5: μ_x^n dependences of the sub-threshold slope of devices with $\sigma_z^n = 11$ nm and $\mu_z^p = 12$ nm (open squares), $\sigma_z^n = 9.0$ nm and $\mu_z^p = 10$ nm (closed circles), and $\sigma_z^n = 7.0$ nm and $\mu_z^p = 8.0$ nm (open triangulars). The parameter μ_x^p is adjusted to obtain $I_{off} = 5.45\,\mu$A/μm at $V_g = 0$ V (see Fig. 2).

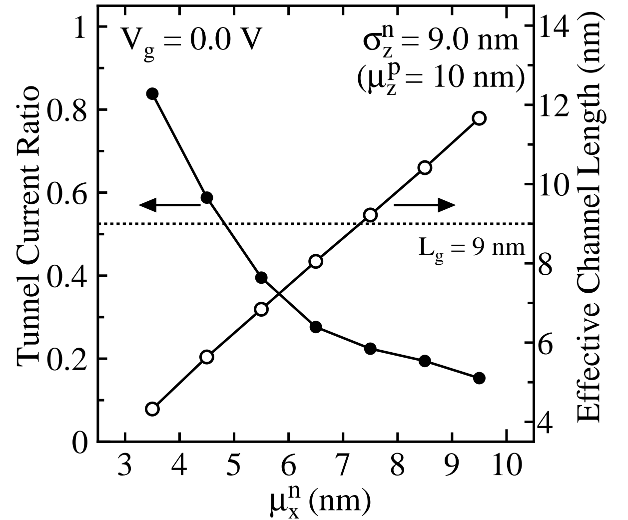

Figure 6: μ_x^n dependence of the SD-tunneling current ratio (closed circles) and the effective channel length (open circles) for $\sigma_z^n = 9.0$ nm and $\mu_z^p = 10$ nm at $V_g = 0$ V. Dotted line indicates the gate length $L_g = 9.0$ nm.

From Fig. 7, we see that I_{on} becomes maximum at $\mu_x^n = 6.5$ nm, and the maximum I_{on}/I_{off} ratios of 50, 54 and 57 are achieved for $\sigma_z^n = 11$, 9.0, and 7.0 nm, respectively. For smaller μ_x^n, a high channel barrier with high p-type concentrations at the channel region is required in order to obtain the fixed off-current $I_{off} = 5.45\,\mu$A/μm because of the large SD-tunneling current. As a result, effects of the subband channel barrier lowering by the gate electric field are less significant than that in the device with larger μ_x^n at the on-state. As seen in Fig. 8, where we plot E_{top} versus μ_x^n

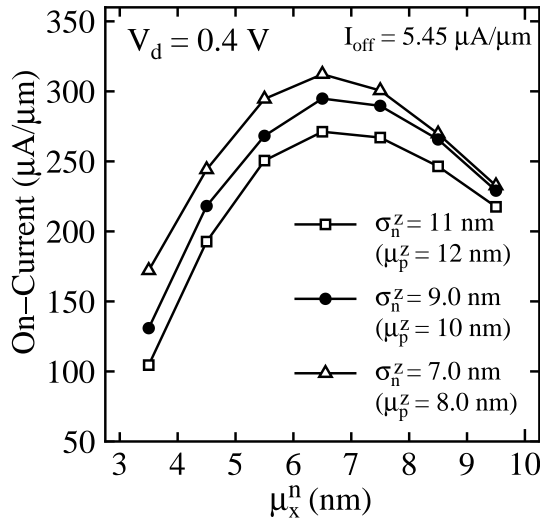

Figure 7: μ_x^n dependence of I_{on} at $V_g = 0.4$ V of the devices with $\sigma_z^n = 11$ nm (squares), $\sigma_z^n = 9.0$ nm (circles), and $\sigma_z^n = 7.0$ nm (triangulars). The parameter μ_x^p is adjusted so as to obtain $I_{\text{off}} = 5.45\,\mu$A/$\mu$m at $V_g = 0$ V.

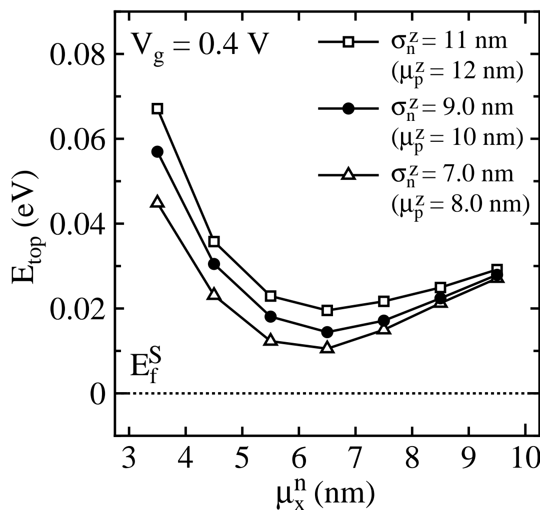

Figure 8: The maximum energies of the channel barrier, E_{top}, versus μ_x^n at the on-state ($V_g = 0.4$ V). Doping parameters are the same as those in Fig. 7. Dotted line represents $E_f^S = 0$ eV.

at $V_g = 0.4$ V, the channel barrier remains high for smaller μ_x^n. For the same reason, lager I_{on} is obtained for smaller σ_z^n. On the other hand, for larger μ_x^n, because the effective channel length becomes longer than $L_g = 9.0$ nm as shown in Fig. 6, there are some parts of the channel barrier region which cannot be controlled by the gate electric field. This gate uncontrollable channel barrier suppresses E_{top} lowering at the on-state, resulting in degradation of the on-current characteristics.

4 Conclusion

We have investigated the doping profile effects on the device characteristics of sub-10 nm gate length bulk n-MOSFET by performing the NEGF transport simulation of bulk-MOSFETs with various doping profiles. We find that n-type offset doping for source/drain regions can significantly suppress the SD-tunneling current. The reduction of the SD-tunneling current by the off-set doping profile is effective to achieve large $I_{\text{on}}/I_{\text{off}}$ ratio. However, excessive off-set n-type doping degrades the on-current characteristics due to the existence of the gate uncontrollable channel barrier. Consequently, the best device characteristics have been obtained for the $\mu_x^n = 6.5$ nm off-set doping profile in the simulated $L_g = 9.0$ nm bulk n-MOSFETs. We also find that the device characteristics can be improved by the shallow doping profile, although the difference of the doping profile along the z-direction have little effects on the device characteristics of ultra-small devices.

Acknowledgment

We would like to thank Semiconductor Technology Academic Research Center (STARC) for financial support.

References

[1] H. Wakabayashi, S. Yamagami, N. Ikezawa, A. Ogura, M. Narihiro, K. Arai, Y. Ochiai, K. Takeuchi, T. Yamamoto, and T. Mogami, IEDM Tech. Dig., 989 (2003).

[2] B. Doris, M. Ieong, T. Kanarsky, Y. Zhang, R.A. Roy, O. Dokumaci, Z. Ren, F.-F. Jamin, L. Shi, W. Natzle, H.-J Huang, J. Mezzapelle, A. Mocuta, S. Womack, M. Gribelyuk, E.C. Jones, R.J. Miller, H.P. Wong, and W. Haensch, IEDM Tech. Dig., 267 (2002).

[3] H. Kawaura and T. Baba, Jpn. J. Appl. Phys., **42**, 351 (2003).

[4] H.-S. P. Wong, IBM J. Res. & Dev. **46**, 133 (2002).

[5] J.-P. Colinge, Solid-State Electron., **48**, 897 (2004).

[6] J. Kretz, L. Dreeskornfeld, R. Schröter, E. Landgraf, F. Hofmann, and W. Rösner, Microelectronic Engineering, **73-74**, 803 (2004).

[7] H. Takeda and N. Mori, Jpn. J. Appl. Phys. **44**, 2664 (2005).

[8] R. Venugopal, S. Goasguen, S. Datta, and M.S. Lundstrom, J. Appl. Phys., **95**, 292 (2004).

[9] M. Ogawa, H. Tsuchiya, and T. Miyoshi, IEICE. Trans. Electron., **E86-C**, 363 (2003).

[10] D.A. Antoniadis, I.J. Djomehri, K.M. Jackson, and S. Miller, http://www-mtl.mit.edu:/researchgroups/Well/.